ROYAL SOCIETY
OF CHEMISTRY

COMMUNICATION

CrossMark
click for updates

Pseudomorphic-phase transformation of NiCo based ternary hierarchical 2D-1D nanostructures for enhanced electrocatalysis†

Wei Yang Lim,[a] Yee Fun Lim[b] and Ghim Wei Ho[*abc]

While electrochemical water splitting is one of the most promising methods to store electrical energy in chemical bonds, facile fabrication of transition metal electrocatalyst materials with judicious chemical and structural design to facilitate high electrochemical reactivity with an in-built gas bubble release mechanism is currently lacking. Here, a facile pseudomorphic-phase transformation of a diversified ternary NiCo hierarchical structure is demonstrated. Essentially, a universal template of hydroxide derivatives facilitates successive pseudomorphic-phase transformation with structural framework preservation. Direct growth of integrated 2D nanosheet-1D nanowire hierarchical features onto a conductive electrode leads to strong interfacial contact and an extended platform for electrolyte accessibility as well as provision of a discontinuous surface for low adhesion gas bubble evolution. Collectively, the as-prepared mixed transition metal and multi-dimensional structured electrode presents a uniquely advantageous electrochemical energy conversion material design.

Recently, low cost and earth abundant mixed transition metal hydroxides, oxides and sulfides have gained much research attention as promising substitutes for rare/noble metal based catalysts.[1–5] Such mixed transition composite materials have been demonstrated to overcome the drawbacks of single material constitution, as they combine the beneficial properties of individual compositions for potential synergistic effects. Among transition metals, Co based materials have been considered as promising electrocatalysts because of their environmental benignity and high catalytic activity.[1,6] To further enhance their electrochemical activity, Ni atoms are

incorporated into Co based electrode materials to increase the density of catalytically active sites. Such ternary composites have shown substantially enhanced electrical conductivity and electrochemical performance by at least two orders of magnitude higher than individual binary nickel or cobalt material.[3,7]

Besides chemical composition consideration, structural design and integrity, issues that hamper further advances in electrocatalytic activity demand research exploration. Inappropriate structural design and poor structural integrity lead to corresponding suppressed gas evolution and limited cycling stability. In particular, aggregated and planar-oriented nanowires/nanosheets generally offer limited accessibility to active sites constrained to the outerlying material in contact with the electrolyte. Moreover, gas bubbles produced during electrocatalysis have an inclination to adhere onto planar surfaces, leading to an undue ohmic drop. This is attributed to the restricted contact between the catalyst and electrolyte.[8,9] In contrast, well-assembled nanowire or nanosheet arrays enhance ionic diffusion and facilitate ionic transport to the interior part of electrodes and hence increase utilization of electrode materials.[10] Furthermore, well-assembled hierarchical nanostructures favor gas bubble de-pinning or effective wicking of small bubbles. This ensures non-limiting electrolyte diffusion especially at high current densities and vigorous gas evolution conditions.[6] Another concern is associated with the preparation of these hierarchical nanostructures which usually prevail in powder forms that are subsequently bonded to conductive substrates. This poses challenges to the stability and electrical conductivity of the electrode. Essentially, the instability emerges from electrocatalyst powder detaching from the substrates concurrently with the reduced conductivity arising from the use of electrical insulating binders.

Herein we report pseudomorphic retention with topotactic transformation of a diversified ternary NiCo hierarchical structure comprising dissimilar low-dimensional structures *i.e.* 2D nanosheets-1D nanowires. Explicitly, the base structural units of hydroxide intermediates serve as a universal template for the successive phase transformation of various NiCo based

[a]Department of Electrical and Computer Engineering, National University of Singapore, 4 Engineering Drive 3, Singapore 117583. E-mail: elehgw@nus.edu.sg

[b]Engineering Science Programme, National University of Singapore, 9 Engineering Drive 1, Singapore 117575

[c]Institute of Materials Research and Engineering, A*STAR (Agency for Science, Technology and Research), 2 Fusionopolis Way, Singapore 138634

ternary materials while concomitantly warranting structural framework retention. The anchored base growth of the ternary NiCo hierarchical structure provides strong interfacial contact with a conductive electrode. More importantly, the synergistic vertically orientated 2D nanosheets integrated with abundant 1D nanowire nanoarrays offer extended edge sites and provide an in-built discontinuous architecture that promotes low adhesion gas bubble evolution. Having such a proposed non-planar 2D nanosheet-1D nanowire hierarchical design strategy has markedly enhanced the electrochemical activity and stability, granting a highly favorable electrochemical energy conversion material system.

As shown in Fig. 1a, 2D nanosheet-1D nanowire nickel cobalt hydroxide composite intermediates (NC–H) were first synthesized and then utilized as the template for subsequent pseudomorphic-phase transformation. An understanding of the formation of this unique hierarchical structure that comprises two dissimilar low-dimensional structures is established by investigating the morphological evolution at 3, 5 and 10 h as shown in Fig. 1b–d, respectively. Initially, 2D hexagonal nanosheets are formed and at 3 h duration short 1D nanowires are observed to grow on the 2D hexagonal nanosheets. The nanowires are found to extend outwardly not only on the basal planes but also at the edges of the 2D hexagonal nanosheets. After a prolonged growth of 10 h, the nanowires become noticeably elongated and populated to yield a 2D nanosheet-1D nanowire hierarchical structure, with nanosheets 150 nm in thickness and 6–8 μm in size as well as nanowires 500–800 nm in length and 150 nm in diameter.

The synthesis is carried out in aqueous solution. Ammonium fluoride dissociates to induce fluoride media, while cobalt and nickel nitrate dissolve as respective ion sources.
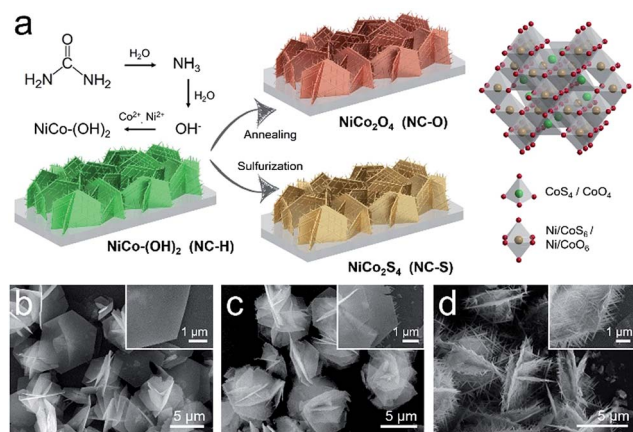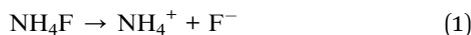
$$NH_4F \rightarrow NH_4^+ + F^- \tag{1}$$

$$Ni(NO_3)_2 \rightarrow Ni^{2+} + 2NO_3^- \tag{2}$$

$$Co(NO_3)_2 \rightarrow Co^{2+} + 2NO_3^- \tag{3}$$

During the growth process, a urea hydrolysis reagent and hydroxide anions are produced to precipitate cobalt and nickel ions into a hydroxide composite.

$$CO(NH_2)_2 + H_2O \rightarrow 2NH_3 + CO_2 \tag{4}$$

$$NH_3 + H_2O \rightarrow NH_4^+ + OH^- \tag{5}$$

$$Co^{2+} + Ni^{2+} + 2OH^- \rightarrow NiCo(OH)_2 \tag{6}$$
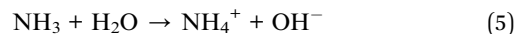
Typically, ammonium fluoride plays two vital roles in the formation of the well-crystalline hierarchical nanostructure: firstly as a structure directing agent and secondly as a crystal forming agent.[11–13] To validate the hypothesis, NiCo–(OH)$_2$ is synthesized without ammonium fluoride. Consequently, self-assembled microspheres comprise 1D nanowires that are synthesized instead of a 2D nanosheet-1D nanowire hierarchical structure (Fig. S1†).

Besides the homogeneous nucleation and precipitation of a 2D nanosheet-1D nanowire hierarchical structure in powder form, direct growth of the same structure with an anchored base onto conducting Ni foam is also attempted. Evidently, similar 2D nanosheet-1D nanowire NC–H is observed at 10 h growth duration. The nanostructures are vertically orientated and well-assembled uniformly throughout the Ni foam (Fig. 2a and b). Similarly, vertically-aligned 2D nanosheets with the absence of 1D nanowires are seen at 3 h growth (Fig. S2†). Under TEM inspection, it can be seen that the hierarchical structure consists of 2D nanosheets with numerous 1D nanowires nucleated at the edge and basal planes of the nanosheets (Fig. 2d). The HRTEM images of the nanosheets and nanowires in the marked regions of Fig. 2c and e, respectively, show single-crystal features. Both HRTEM images depict a lattice spacing of 0.27 nm, corresponding to the interplanar distance of (101) of NiCo–(OH)$_2$ composites which suggests homoepitaxial growth of 1D nanowires on 2D nanosheets.[14–16] Additionally,

Fig. 1 (a) Schematic diagram of hydroxide intermediate (NC–H) synthesis and consequent pseudomorphic-phase transformation to NC–O and NC–S. Morphological evolution of NC–H at (b) 3, (c) 5 and (d) 10 h. Insets magnify the edges of the corresponding nanosheets.
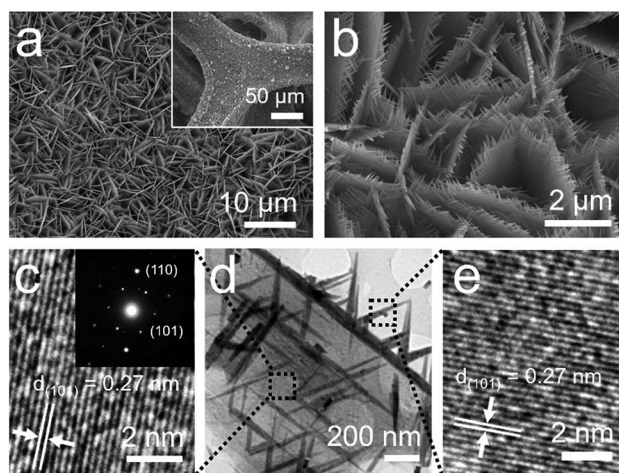
Fig. 2 (a and b) SEM and (d) TEM images of NC-H grown on Ni foam. HRTEM images of the (c) nanosheets and (e) nanowires, showing clear lattice fringes with a 0.27 nm spacing, corresponding to an interplanar distance of (101) of NiCo–(OH)$_2$ composites. Inset of (c) is the SAED pattern from the nanosheet.

homogenous dispersion of Ni, Co and O elements are detected using energy dispersive X-ray mapping (Fig. S3†), which suggests the formation of a uniform composite without any phase separation/segregation. Collectively, these observations affirm the construction of high-quality homogenous NiCo–(OH)$_2$ hierarchical structures as a prospective template for the subsequent pseudomorphic-phase transformation of ternary NiCo composites.

Facile phase transformation of NiCo hydroxides (NC–H) into NiCo oxide (NC–O) and NiCo sulfide (NC–S) is achieved through successive annealing and sulfurization processes, respectively. Accordingly, drastic color switches from purplish NC–H to blackish NC–O and NC–S attest the formation of new compositions (Fig. S4†). The crystallographic structures and chemical composition of the specimens are depicted in Fig. 3a and b. The diffraction peaks of NC–H are in good agreement with the literature reports of the hydroxide composite α-Co(OH)$_2$ (JCPDS no. 74-1057) and α-Ni(OH)$_2$ (JCPDS no. 38-0715) phase.[16,17] The diffraction peaks of NC–O and NC–S can be indexed to cubic NiCo$_2$O$_4$ (JCPDS no. 73-1702)[18] and cubic NiCo$_2$S$_4$ (JCPDS no. 43-1477)[19] phases, respectively. The spinel structure of NiCo$_2$O$_4$ and NiCo$_2$S$_4$ with space group $Fd3m$ is schematically illustrated in Fig. 1a.[20,21] It can be seen that Ni atoms are embedded in the octahedron and the Co atoms are located in both octahedral and tetrahedral sites.[20] Accordingly, the XPS spectra of NC–H (Fig. 3b and S5†) match the literature report of NiCo–(OH)$_2$ composites.[22] As such, the O 1s peak centered at 531.1 eV is commonly associated with bonded oxygen attributed to the hydroxyl group.[23] In contrast to the O 1s spectrum of NC–O, the hydroxyl-associated O 1s peak is quenched after the annealing process, while two deconvoluted peaks at 532.7 eV and 528.9 eV ascribed to the oxygen species in the surface-adsorbed H$_2$O molecules and metal–oxygen bond (M–O) respectively are observed.[23] In the case of NC–S, the core-level spectrum of the S

2p spectrum is deconvoluted into three peaks accompanied with a shake-up satellite peak at 168.8 eV. Besides the S 2p$_{3/2}$ and 2p$_{1/2}$ peaks at 162.8 eV and 161.5 eV respectively, the peaks at 162.6 eV and 163.8 eV can be assigned to low coordination sulfur ions at the surface and metal–sulfur bond (M–S), respectively.[24,25] Combining the evidence of M–O and M–S bonds with those of predominant Ni^{2+} and Co^{3+} states from Ni 2p and Co 2p spectra (Fig. S6†),[24] the formation of NiCo$_2$O$_4$ and NiCo$_2$S$_4$ is evidently presented.

Other than the complete compositional transformations, the morphologies of NC–O and NC–S retain the 2D nanosheet-1D nanowire of the NC–H hierarchical structure (Fig. S7†). This phase conversion strategy exploits the intrinsically layered structure of hydroxide for self-templated transformation of oxide and sulfide composites with well-preserved structures. The self-templating method, in which the template itself is involved as a reactant, has the advantage of no additional template removal requirement. Moreover, the EDX elemental mapping of NC–S, shown in Fig. 3c and close inspections of NC–O and NC–S with HRTEM (Fig. S8 and S9†) further verify the retention of the single crystal feature and homogenous phase composition of the hierarchical structure.[24,26] Appropriately, these exclusive characteristics can be highlighted as pseudomorphic-phase transformations, which can be accredited to the establishment of a robust NC–H template endowed with exceptional structural homogeneity and crystallinity. This approach brings about not only an unrestrictive pathway for the preparation of a diversified ternary compound, but more importantly systematic comparison of merely a chemical composition aspect in regard to electrochemical performances can be achieved.

It can be recognized that the NC–H self-templated phase transformation approach can be engaged as a convenient fabrication method of efficient electrocatalysts. This is due to its facile ternary composition control and direct substrate growth capability as well as a favorable hierarchical design. The direct growth of hierarchical arrays onto the underlying conductive current collector ensures good electrical conductivity as well as high structural stability. Also, the 2D vertically aligned nanosheet design warrants efficient mass transport and accessibility to active surfaces. Besides, the 1D nanowires offer additional catalytically active edges and a discontinuous triple phase contact line (solid-liquid-gas) for efficient gas evolution.

Subsequently, hydrogen evolution reaction (HER) activities obtained using linear sweep voltammetry (LSV) under an acidic solution (0.5 M H$_2$SO$_4$) in a standard three-electrode electrochemical configuration are shown in Fig. 4a. It is apparent that among all three nanostructured electrodes, the HER activity of NC–S surpasses that of the NC–O and the NC–H. Quantitatively, the overpotentials of NC–S at current densities of 10 mA cm^{-2} and 100 mA cm^{-2} are determined to be 155 mV and 327 mV, while those of NC–O are 223 mV and 489 mV and NC–H are 222 mV and 516 mV, respectively. In addition, their kinetic activities are estimated based on Tafel plots in Fig. 4b. The corresponding Tafel slopes of NC–S, NC–O and NC–H are 88, 123 and 130 mV dec^{-1}. In order to gain further insight on the HER superiority of NC–S over NC–O and NC–H, they were further assessed through
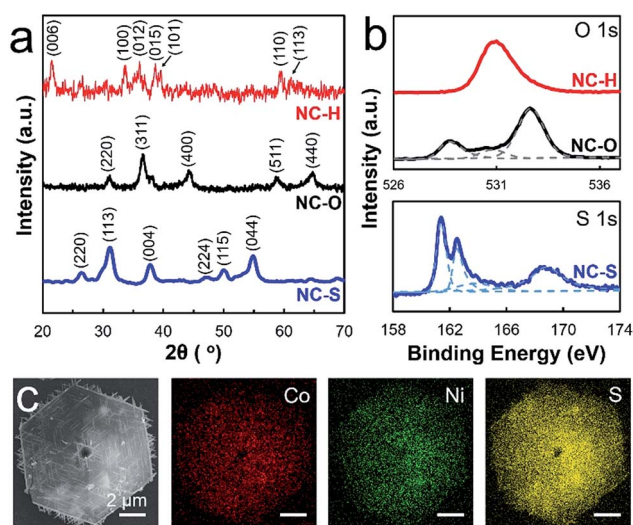
Fig. 3 (a) XRD patterns of NC–H, NC–O and NC–S. (b) XPS O 1s core-level spectra of NC–H and NC–O, and S 1s spectrum of NC–S, respectively. (c) EDX mapping of NC–S with uniformly distributed Co, Ni and S elements.

This journal is © The Royal Society of Chemistry 2017

J. Mater. Chem. A, 2017, **5**, 919–924 | **921**
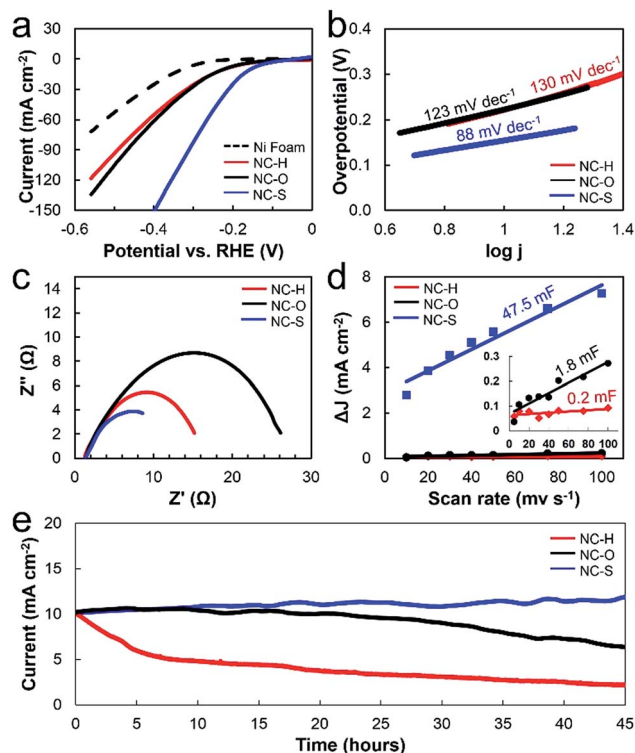
Fig. 4 (a) Linear sweep voltammetry (LSV) curves of nickel foam and nickel foam grown with NC–H, NC–O and NC–S, respectively, toward the HER in an acidic electrolyte of 0.5 M H_2SO_4. (b) Tafel plots of NC–H, NC–O and NC–S. (c) Electrochemical impedance spectra (EIS) of the catalysed HER at an overpotential of 100 mV. (d) Electrochemical surface area (ECSA) measurements of NC–H, NC–O and NC–S, represented by the linear slopes which are equivalent to twice the double-layer capacitance, C_{dl}. (e) Chronopotentiometry test (i–t curve) of NC–H, NC–O and NC–S in an acidic electrolyte of 0.5 M H_2SO_4 at a current density of 10 mA cm^{-2} up to 45 h for stability assessment.

other electrochemical characterization, *i.e.* electrochemical impedance spectroscopy (EIS) for the electron transport as well as cyclic voltammetry (CV) for the electrochemical double layer capacitance. For the EIS measurement (Fig. 4c), the semicircle curves can be simply fitted with an equivalent circuit consisting of a resistor (R_s) in series with a parallel combination of a resistor (R_{ct}) and a constant phase element, in which R_s and R_{ct} represent the contact resistance and the charge transfer resistance, respectively.[27] All NC–H, NC–O and NC–S show comparable series resistance R_s (high frequency intercept on the real axis); however their charge-transfer resistances R_{ct} (radius of the semicircle on the real axis) differ substantially, specifically 7.4 Ω, 13.2 Ω and 5.5 Ω. This may imply that the M–S bonds facilitate effective electron transport and hence greatly augment their electrocatalytic performance.[28] The capacitance values of NC–H, NC–O and NC–S are determined from the linear relationship of current density difference in anodic and cathodic current scan *versus* scan rates,[29] shown to be 0.2 mF, 1.8 mF and 47.5 mF, respectively (Fig. 4d). Typically, metal–sulphide (M–S) bonds possess larger bond lengths as compared to metal–oxide (M–O) bonds.[30–33] The greater bond length facilitates electron localization on the sulfur moieties, favoring the adsorption of

hydrogen (H_{ads}) and reducing the kinetic energy barrier for subsequent transformation of H_{ads} into H_2.[30,34] Hence, NC–S shows a much higher ECSA value than NC–OH and NC–O, and reveals the higher electrocatalytic activity of sulfur moieties over its hydroxyl and oxygen counterparts.[28]

Catalytic stability is an important performance metric of electrocatalysts. Hence, chronoamperometry measurements are used to investigate the stability under prolonged electrolysis. The stability of NC–H, NC–O and NC–S is studied for 45 h under constant voltage mode in acidic electrolytes, whereby specific applied voltage is chosen to yield a current density of 10 mA cm^{-2}. From Fig. 4e, it can be seen that the NC–H current yield decreases at the start of the stability test. Comparatively, NC–O has relatively higher stability as it shows a constant current yield up to 10 h, after which it degrades. However, NC–S shows noticeably high consistency in current yield over the entire 45 h duration and beyond (Fig. S10†). The current yields of NC–H, NC–O and NC–S are 2.2, 6.4 and 11.8 mA cm^{-2}, indicating 78, 36 and 0% deterioration of electrocatalytic activity after 45 h, respectively. It is noted that the 2D-1D hierarchical structures of all three compounds remained largely intact after 45 h of H_2 evolution during the stability testings (Fig. S11†). In addition, the stability performance of NC–H, NC–O and NC–S in a basic electrolyte is also obtained as shown in Fig. S12.† Consistently, the metal sulfide structure exhibits an outstanding and stable HER electrocatalyst. A comparison of NC–S against other HER electrocatalysts is tabulated as Table S1,† with all their respective morphologies, electrolytes, overpotentials at 10 mA cm^{-2}, Tafel slopes and stabilities listed.

The hierarchical structure provides a high-degree discontinuous triple phase contact line. Consequently, gas bubbles exhibit lower adhesion force to the electrode and evolve at a smaller critical diameter.[6,8,35] To illustrate the bubble depinning effect of the hierarchical structure, electrocatalytic activities of NC–S with 2D nanosheet-1D nanowire and NC–S with solely 2D nanosheets (NC–S2) (Fig. S13†) are evaluated using LSV. The HER of NC–S clearly outperforms the NC–S2 especially in the high current density region (Fig. 5a). This suggests effective wicking of the as-formed gas bubbles on the hierarchical structure under vigorous gas evolution conditions. Hence, it ensures a non-limiting electrolyte diffusion and effective mass transfer between the contact working area of the electrolyte and electrode.[6] In contrast, plain 2D nanosheets exhibit an impeded electrochemical activity which may be attributed to the reduced working area of the electrode due to the creation of a "dead zone" by the adhered gas bubbles.[6,8,30] Subsequently, frame shots of gas bubble evolution on NC–S and NC–S2 operated at 0.4 V were captured using a high speed camera as shown in Fig. 5b and c, respectively. The average bubble diameters of NC–S and NC–S2 that can be resolved in the current high-speed camera setup are 35 and 163 μm, respectively. This demonstrates that the in-built structural design of NC–S is capable of self-releasing the gas bubbles from the electrodes at a relatively smaller diameter. At lower magnification (Fig. 5b and c insets), it can be observed that larger gas bubbles are noticeably pinned/adhered onto the NC–S2 electrode as compared to the NC–S electrode. The relationship between nanostructured electrode design and bubble evolution

922 | *J. Mater. Chem. A*, 2017, **5**, 919–924

This journal is © The Royal Society of Chemistry 2017
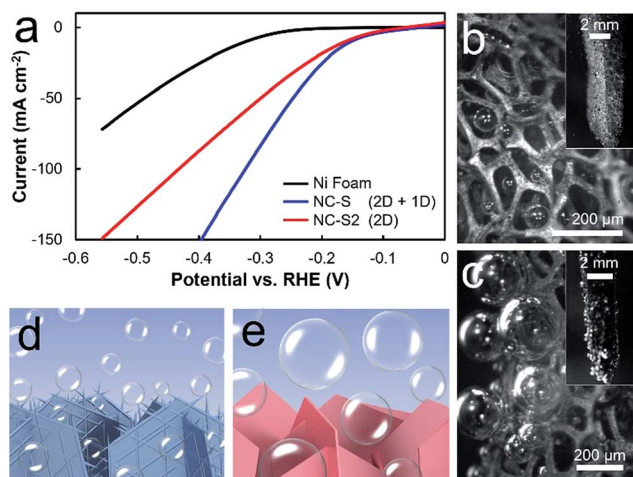
Fig. 5 (a) LSV of NC−S (2D nanosheets-1D nanowires) and NC−S (2D nanosheets) toward the HER in acidic electrolytes of 0.5 M H_2SO_4. Frame shots of bubble evolution on (b) NC−S and (c) NC−S2 electrodes. (d and e) Schematics of the relationship between the structural design and gas bubble evolution effects.

effects are schematically illustrated in Fig. 5d and e. The LSV current density and gas bubble behavior findings suggest a considerable bubble depinning effect originating from the befitting hierarchical architecture of the electrode.

Conclusions

In summary, this work demonstrates the ability to perform pseudomorphic-topotactic transformation of a diversified ternary NiCo hierarchical structure comprising a hybrid 2D nanosheet-1D nanowire structure. Notably, a facile structural modulation strategy is proposed *via* phase transformation of a hydroxide intermediate template into diverse NiCo composites. This warrants structural framework preservation and comparative electrochemical investigations of the various NiCo based ternary materials. Interestingly, the well-assembled and upright orientation of the hierarchical structure provides high accessibility of electrolyte to abundant edge sites accompanied by low adhesion rapid release of the as-formed gas bubbles. The facile synthesis of various 2D-1D ternary metal composites combined with their superior electrocatalysis performance, is anticipated to advance the exploration of multi-compositional/dimensionally hierarchical nanostructures for energy generation applications and beyond.

Acknowledgements

Notes and references

1   P. D. Tran, S. Y. Chiam, P. P. Boix, S. S. Pramana, J. Fize, V. Aetero and J. Barber, *Energy Environ. Sci.*, 2013, **6**, 2452–2459.

2   X. Long, G. Li, Z. Wang, H. Zhu, T. Zhang, S. Xiao, W. Guo and S. Yang, *J. Am. Chem. Soc.*, 2015, **137**, 11900–11903.

3   S. Baranton and C. Coutanceau, *Appl. Catal., B*, 2013, **136–137**, 1–8.

4   H. Wang, H.-W. Lee, Y. Deng, Z. Lu, P.-C. Hsu, Y. Liu, D. Lin and Y. Cui, *Nat. Commun.*, 2015, **6**, 7261.

5   J. Li, Y. Wang, T. Zhou, H. Zhang, X. Sun, J. Tang, L. Zhang, A. M. Al-Enizi, Z. Yang and G. Zheng, *J. Am. Chem. Soc.*, 2015, **137**, 14305–14312.

6   M. S. Faber, R. Dziedzic, M. A. Lukowski, N. S. Kaiser, Q. Ding and S. Jin, *J. Am. Chem. Soc.*, 2014, **136**, 10053–10061.

7   K. K. Lee, W. S. Chin and C. H. Sow, *J. Mater. Chem. A*, 2014, **2**, 17212–17248.

8   Z. Lu, W. Zhu, X. Yu, H. Zhang, Y. Li, X. Sun, X. Wang, H. Wang, J. Wang, J. Luo, X. Lei and L. Jiang, *Adv. Mater.*, 2014, **26**, 2683–2687.

9   S. H. Ahn, I. Choi, H.-Y. Park, S. J. Hwang, S. J. Yoo, E. Cho, H.-J. Kim, D. Henkensmeier, S. W. Nam, S. Kim and J. H. Jang, *Chem. Commun.*, 2013, **49**, 9323–9325.

10 Y. Yan, L. Thia, B. Y. Xia, X. Ge, Z. Liu, A. Fisher and X. Wang, *Adv. Sci.*, 2015, **2**, 1500120.

11 J. Wang, L. Deng, G. Zhu, L. Kang, Z. Lei and Z.-H. Liu, *CrystEngComm*, 2013, **15**, 6682–6689.

12 A. Kuperman, S. Nadimi, S. Oliver, G. A. Ozin, J. M. Garces and M. M. Olken, *Nature*, 1993, **365**, 239.

13 J. Arichi and B. Louis, *Cryst. Growth Des.*, 2008, **8**, 3999–4005.

14 H. Wang, J. Gao, Z. Li, Y. Ge, K. Kan and K. Shi, *CrystEngComm*, 2012, **14**, 6843–6852.

15 Y. Bai, W. Liu, C. Yu, T. Wang, J. Feng and S. Xiong, *J. Phys. Chem. C*, 2016, **120**, 2984–2992.

16 J. Pu, Y. Tong, S. Wang, E. Sheng and Z. Wang, *J. Power Sources*, 2014, **250**, 250–256.

17 L. Huang, D. Chen, Y. Ding, S. Feng, Z. L. Wang and M. Liu, *Nano Lett.*, 2013, **13**, 3135–3139.

18 T. Zhu, E. R. Koo and G. W. Ho, *RSC Adv.*, 2015, **5**, 1697.

19 H. Chen, J. Jiang, L. Zhang, H. Wan, T. Qia and D. Xia, *Nanoscale*, 2013, **5**, 8879–8883.

20 J. Wu, P. Guo, R. Mi, X. Liu, H. Zhang, J. Mei, H. Liu, W.-M. Lau and L.-M. Liu, *J. Mater. Chem. A*, 2015, **3**, 15331.

21 C. Xia, P. Li, A. N. Gandi, U. Schwingenschlögl and H. N. Alshareef, *Chem. Mater.*, 2015, **27**, 6482–6485.

22 J. Liang, R. Ma, N. Iyi, Y. Ebina, K. Takada and T. Sasaki, *Chem. Mater.*, 2010, **22**, 371–378.

23 C. Xiao, Y. Li, X. Lu and C. Zhao, *Adv. Funct. Mater.*, 2016, **26**, 3515–3523.

24 A. Sivanantham, P. Ganesan and S. Shanmugam, *Adv. Funct. Mater.*, 2016, **26**, 4661–4672.

25 X. Wu, S. Li, B. Wang, J. Liu and M. Yu, *Phys. Chem. Chem. Phys.*, 2016, **18**, 4505–4512.

26 W.-M. Liu, T.-T. Gao, Y. Yang, Q. Suna and Z.-W. Fu, *Phys. Chem. Chem. Phys.*, 2013, **15**, 15806–15810.

27 J. Wang, H.-X. Zhong, Z.-L. Wang, F.-L. Meng and X.-B. Zhang, *ACS Nano*, 2016, **10**, 2342–2348.

28 Y. Liu, Y. Li, H. Kang, T. Jin and L. Jiao, *Mater. Horiz.*, 2016, **3**, 402–421.

29 C. W. Li, J. Ciston and M. W. Kanan, *Nature*, 2014, **508**, 504–507.

This journal is © The Royal Society of Chemistry 2017

J. Mater. Chem. A, 2017, **5**, 919–924 | 923

30 G.-F. Chen, T. Y. Ma, Z.-Q. Liu, N. Li, Y.-Z. Su, K. Davey and S.-Z. Qiao, *Adv. Funct. Mater.*, 2016, **26**, 3314–3323.

31 W. Liu and H. H. Thorp, *Inorg. Chem.*, 1993, **32**, 4102–4105.

32 M. K. Aydinol, A. F. Kohan, G. Ceder, K. Cho and J. Joannopoulos, *Phys. Rev. B*, 1997, **56**, 1354.

33 N. Kornienko, J. Resasco, N. Becknell, C.-M. Jiang, Y.-S. Liu, K. Nie, X. Sun, J. Guo, S. R. Leone and P. Yang, *J. Am. Chem. Soc.*, 2015, **137**, 7448–7455.

34 C.-J. Chen, P.-T. Chen, M. Basu, K.-C. Yang, Y.-R. Lu, C.-L. Dong, C.-G. Ma, C.-C. Shen, S.-F. Hu and R.-S. Liu, *J. Mater. Chem. A*, 2015, **3**, 23466–23476.

35 Z. Lu, Y. Li, X. Lei, J. Liu and X. Sun, *Mater. Horiz.*, 2015, **2**, 294–298.